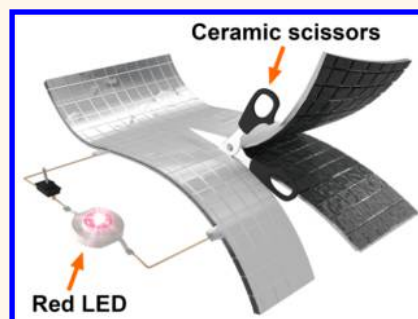


Shape-Tailorable Graphene-Based Ultra-High-Rate Supercapacitor for Wearable Electronics

Binghe Xie,[†] Cheng Yang,^{*,†} Zhexu Zhang,[†] Peichao Zou,[†] Ziyin Lin,[‡] Gaoquan Shi,[§] Quanhong Yang,[†] Feiyu Kang,[†] and Ching-Ping Wong[‡]

[†]Division of Energy and Environment, Graduate School at Shenzhen, Tsinghua University, Shenzhen 518055, People's Republic of China, [‡]School of Materials Science and Engineering, Georgia Institute of Technology, 771 Ferst Drive, Atlanta, Georgia 30332, United States, and [§]School of Chemistry, Tsinghua University, Beijing 100084, People's Republic of China

ABSTRACT With the bloom of wearable electronics, it is becoming necessary to develop energy storage units, *e.g.*, supercapacitors that can be arbitrarily tailored at the device level. Although gel electrolytes have been applied in supercapacitors for decades, no report has studied the shape-tailorable capability of a supercapacitor, for instance, where the device still works after being cut. Here we report a tailorable gel-based supercapacitor with symmetric electrodes prepared by combining electrochemically reduced graphene oxide deposited on a nickel nanocone array current collector with a unique packaging method. This supercapacitor with good flexibility and consistency showed excellent rate performance, cycling stability, and mechanical properties. As a demonstration, these tailorable supercapacitors connected in series can be used to drive small gadgets, *e.g.*, a light-emitting diode (LED) and a minimotor propeller. As simple as it is (electrochemical deposition, stencil printing, *etc.*), this technique can be used in wearable electronics and miniaturized device applications that require arbitrarily shaped energy storage units.



KEYWORDS: graphene · supercapacitor · tailorable

Wearable electronic devices are leading the trend of commercial electronics, mainly due to their novel characteristics of flexibility, light weight, and compact size. The energy storage units such as batteries and supercapacitors are critical components of wearable electronics; thus, they have attracted a great deal of attention.^{1–3} From the ergonomic aspect, these energy storage units should be capable of being made into arbitrary shapes, unlike conventional coin, column, or square counterparts, to meet a high level of integration demand and to cater to versatile applications ranging from cloth, to smart glasses, to watches or bracelets.⁴ For this purpose, tailorable energy storage units that can be reshaped or cut at the device level need to be developed. Furthermore, these tailorable energy storage units could serve as reliable power suppliers even if they are damaged, for example, being cut, punctured, or blasted, ensuring that they are able to power electronics under severe conditions.

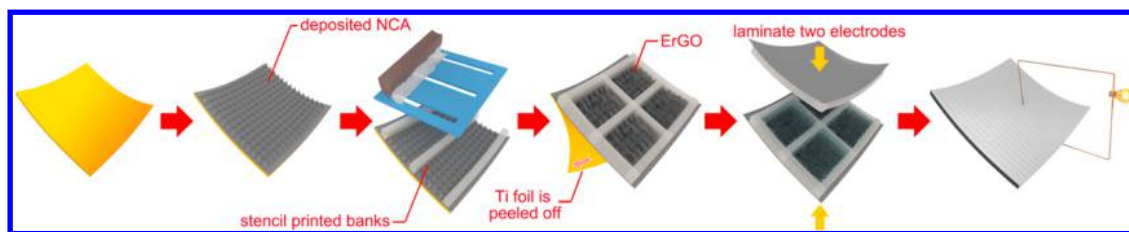
For typical energy storage devices such as lithium ion batteries and supercapacitors, one approach to realize their tailorability is to adopt solid electrolytes. Solid electrolytes can not only provide a strong mechanical support for the device but also prevent the leakage of electrolyte.⁵ For example, Kamaya *et al.* and Mizuno *et al.* recently reported lithium ion batteries with a solid electrolyte, showing improved safety performance.^{6,7} In the past decade, great efforts have also been devoted to all-solid-state supercapacitors.^{8–10} However, supercapacitors with tailorable features have not yet been explored. It should be noted here that the typical ceramic solid electrolyte has an ion mobility about 32–70 times slower than that of a liquid counterpart,¹¹ greatly limiting the power density of the corresponding energy storage device. Additionally, the widely studied gel electrolytes are overwhelmed with weak molecular interactions, which can barely provide enough strength to resist an intense mechanical impact. To date, supercapacitors with both

* Address correspondence to yang.cheng@sz.tsinghua.edu.cn.

Received for review February 8, 2015 and accepted May 4, 2015.

Published online May 04, 2015
10.1021/acsnano.5b00899

© 2015 American Chemical Society



Scheme 1. Schematic illustration of the shape-tailorable graphene-based ultra-high-rate supercapacitor. Regular NCAs deposited on a Ti substrate were used as current collector and then perpendicularly stencil-printed with EVA glue. After constructing the EVA cofferdams, ErGO was electrochemically deposited onto the NCAs, and this ultrathin electrode can be peeled off from the Ti carrier substrate. Two pieces of the same ErGO electrodes coated with Na_2SO_4 -PVA gel electrolyte were hot-laminated together to form a tailorable supercapacitor that can drive the light-emitting diode.

tailorable characteristics and a high power density have not been realized.

Carbon materials have been most widely used as electrode materials of commercial supercapacitors.¹² Recently, graphene has drawn unprecedented attention in both academic and industrial aspects, because of its atom-thick two-dimensional structure, large theoretical specific surface area (SSA, $2675 \text{ m}^2/\text{g}$), and ultrahigh theoretical specific capacitance (550 F/g).¹³ Moreover, many well-engineered graphene-based supercapacitors exhibited negligible losses in their capacitances during ultrafast charging/discharging processes.^{14,15} Particularly, manipulating the orientation and assembly of graphene sheets in the electrodes of supercapacitors can improve the rate performance.^{16–18} For example, a constant electric field is able to trigger the self-assembly and reduction of graphene oxide (GO), rendering the electrochemical reduction of GO.^{19–21} Consequently, electrochemically reduced graphene oxide (ErGO) sheets were deposited on a conductive substrate (acting as the current collector), forming a highly porous structure to improve the performance of the supercapacitor.²²

Here we report a tailorable ultra-high-rate supercapacitor using ErGO as the binder-free electrode material. The ErGO was homogeneously deposited on well-defined nickel nanocone arrays (NCAs) by one-step electrochemical deposition with a two-electrode configuration.^{22,23} The involvement of NCAs can help to improve the loaded mass of the active material and improve the contact between the active material and the current collector, rendering excellent transport of electrons through the whole structure, which is beneficial to deliver high areal specific capacitance and superior cycling stability. The mass loading of ErGO can be further increased by multiple depositions and can reach 0.6 mg/cm^2 , showing leading areal specific capacitance in the ErGO system (57.1 mF/cm^2 at 2 mV/s). In addition, the electrode showed 96.5% capacitance retention after 20 000 cycles of CV scanning at a high scan rate of 1000 mV/s , indicating outstanding cycling stability.^{20,24}

To make the supercapacitor tailorable, we stencil-printed hot-melting glue (ethylene vinyl acetate, EVA, resin) lines (width: 0.25 mm ; distance: 3 mm ;

height: $\sim 0.02 \text{ mm}$) on the NCA current collectors with Ti foil supports in a perpendicular direction as cofferdams (banks). Successively, ErGO active material was deposited and a PVA- Na_2SO_4 gel electrolyte was applied, aiming at promoting the mobility of the ions. Subsequently, two identical electrodes were hot-laminated together, generating numerous isolated small square cells, preventing the contact of the opposite electrodes. Finally, the attached Ti foils were peeled off to minimize the packaging size (Scheme 1). Such a tailorable gel supercapacitor (TGS) with EVA cofferdams showed large areal and volumetric specific capacitances, excellent rate performance, and good cycling stability. In addition, a series of device-level characterizations demonstrated that the TGS has excellent flexibility and mechanical robustness. In terms of potential applications, TGSs are able to drive light-emitting diodes (LEDs) and minimotor propellers, even when they suffer from intense slitting. This technique involves simple processes including electrochemical deposition and stencil printing; thus, it is readily scalable to industrial levels.

RESULTS AND DISCUSSION

The NCAs used as the current collector were prepared by a one-step electrodeposition method. SEM images of the NCAs show that they are morphologically uniform (Figure S1a,b). The NCAs grown vertically on the Ti substrate had an average height of about 800 nm with an aspect ratio close to 4, rendering the surface area of the current collector about 2 times larger than that of a planar Ni plate.²³ The large surface area and the regular surface structure may help to load more active materials. Thanks to their dislocation growth mechanism,²⁵ the rough surfaces of NCAs (Figure S1c,d) can enhance the contact between NCAs and the active material.²³

GO was *in situ* converted to ErGO on NCAs *via* electrochemical deposition using a two-electrode system, forming a uniform layer (Figure S2a). In our experiment, the applied voltages ranged from 2.8 to 3.2 V , and no evolution of hydrogen was observed during this process. Different from the previous works on the preparation of ErGO using the three-electrode configuration (the reduction process takes place on the

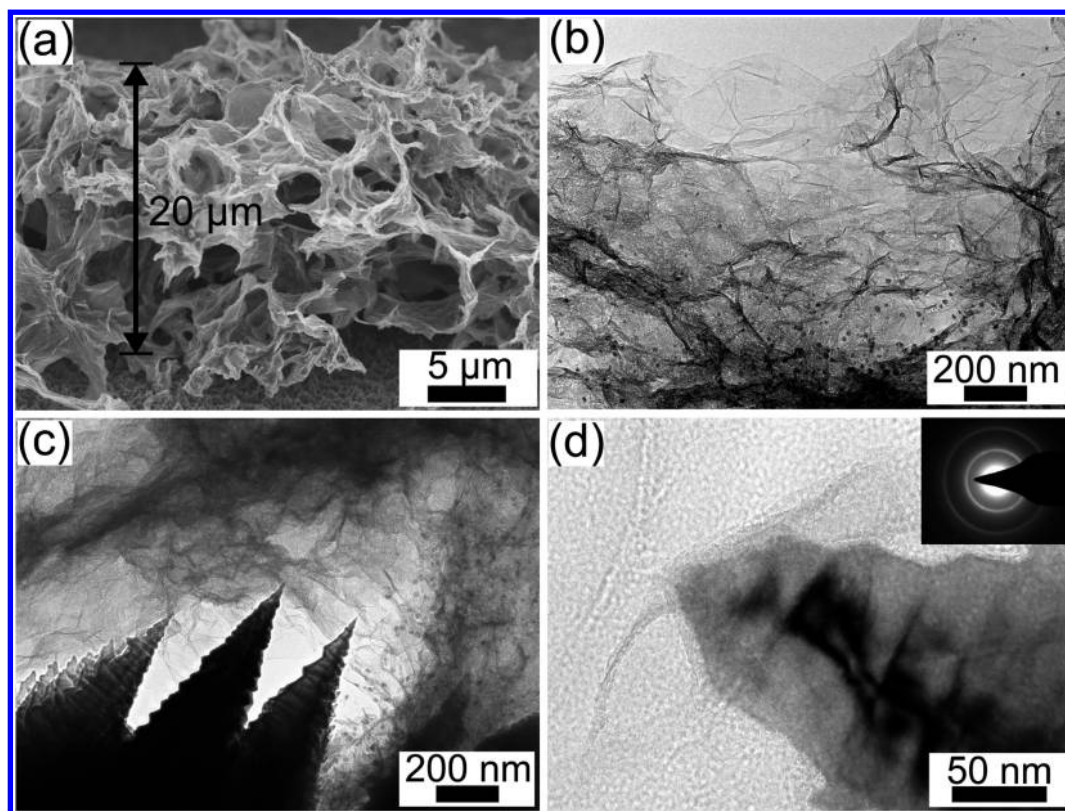


Figure 1. (a) (Side view) SEM image of the macroporous ErGO network (height $\sim 20 \mu\text{m}$) deposited on NCAs at the bottom. (b) TEM image of a thin area of the ErGO network. (c) TEM image of a thin area of the contacting area between ErGO and NCAs. (d) HRTEM image of a nickel nanocone with close contact of ErGO (inset: SAED of the ErGO).

glassy carbon electrode),^{19,21} we adopted the simpler two-electrode method and multiple depositions; thus, we could also obtain ErGO electrodes with large areas (e.g., 24 cm^2 , Figure S2b) and high mass loadings (up to 0.6 mg/cm^2). The formation of ErGO was confirmed by XRD and Raman examinations. As shown in Figure S3a, an intense peak located at $2\theta = 10^\circ$ in the XRD pattern of GO represents the typical structure of the GO sheets, while this peak was replaced by a new one at $2\theta = 26^\circ$ after electrochemical deposition, reflecting the conversion of GO to ErGO.²¹

The FT-IR spectrum of GO shows a broad absorption peak at around 3300 cm^{-1} , which is associated with the hydroxyl groups and carboxylic groups (Figure S3b). The strong peak at approximately $1720\text{--}1740 \text{ cm}^{-1}$ is attributed to the C=O stretching vibrations from carbonyl and carboxylic groups. A weak peak at approximately 1614 cm^{-1} corresponds to the C=C skeletal vibration of the unoxidized graphitic domain. The peak at 1045 cm^{-1} is consistent with a C–O stretching vibration. The spectrum also indicates the presence of O–H bending in tertiary alcohol (1361 cm^{-1}) groups, which were reported to be located on the basal plane of GO.²⁶ After the electrochemical deposition, it is evidenced that the relative intensity of peaks associated with oxygen-containing functional groups was significantly reduced, especially the broad band at around 3300 cm^{-1} . The other peaks originated from a

C–O stretching vibration and a C=C (1614 cm^{-1}) skeletal vibration of the unoxidized graphitic domain. Therefore, most of the oxygen-containing functional groups on the basal plane of GO sheets were removed by electrochemical reduction. A Raman scattering (Figure S3c) investigation showed that the intensity ratio of I_D/I_G increased from 0.97 to 1.16 after the reduction process, which is a typical phenomenon for ErGO and could be attributed to the increased amount of small conjugated domains.²² Additionally, XPS analysis of the C_{1s} of GO and ErGO showed analogous results with a previous report (Figure S4), confirming the reduction process.⁹

In order to construct the supercapacitor device, regular NCAs were grown on a Ti substrate for the current collector, and EVA glue was then stencil-printed on the NCAs to construct the cofferdams. Successively, a macroporous ErGO network was formed on the NCAs by the electrochemical deposition method (Scheme 1). From the top view of ErGO on the NCAs (Figure S5a), the ErGO exhibits a macroporous network characteristic, which is capable of providing fast ion transport channels in the electrode. Cross-sectional observations of the ErGO electrode (Figure 1a) also confirmed that the ErGO can be successfully deposited on the NCAs to form a porous network, and the thickness of ErGO was about $20 \mu\text{m}$. As shown in Figure 1b and Figure S5b, the high-resolution

transmission electron microscopy (HRTEM) analysis showed that the ErGO is high quality; the dark spots may be the residual salt crystals originating from the electrolyte. From Figure 1c,d and Figure S5c,d, it appears that ErGO has good contact with the NCAs, which helps to improve the electron transfer rate. The selected area electron diffraction (SAED) pattern (inset of Figure 1d) of ErGO displays a bright diffraction ring corresponding to the (100) reflection from the graphene plane compared with that of GO (Figure S6), suggesting that the conjugated structure of graphitic domains in GO was recovered.²⁷

In order to evaluate the electrochemical performance of the electrode material, cyclic voltammetry (CV), galvanostatic charging/discharging (GCD), and electrochemical impedance spectroscopy (EIS) analyses were used. All the tests were performed in 0.5 M aqueous Na_2SO_4 electrolyte with a three-electrode configuration. The CV curves over a range of scan rates from 2 to 50 mV/s exhibited an almost ideal symmetric rectangular shape, suggesting the typical capacitive characteristic (Figure S7a). The GCD test was performed with different current densities, over the voltage window of 0 to -0.8 V (Figure S7b).²⁸ The GCD curves kept a nearly ideally triangular shape and exhibited only negligible IR drops of 0.007 V at 0.1 mA/cm^2 and 0.03 V at 1 mA/cm^2 , respectively, by virtue of the good contact between ErGO and NCAs.²³ In addition, the GCD curves of the NCA current collector were recorded under the same current density for ErGO (1 mA/cm^2), demonstrating that the NCA current collector had a negligible contribution to the total capacitance of the electrode (Figure S8). According to eq 1, the maximum areal specific capacitance of the ErGO electrode was close to 57.1 mF/cm^2 at the scan rate of 2 mV/s, which is a leading areal specific capacitance of the ErGO system.^{22,29} With the scan rate increased to 50 mV/s, the areal specific capacitance slightly decreased to 38.8 mF/cm^2 , suggesting an excellent rate performance (Figure S7c). The excellent capacitive property can be mainly attributed to the following two reasons: (1) the macroporous ErGO network facilitates the diffusion of ions from the electrolyte to the inside of the electrodes to form electrical double layers; (2) the involvement of the NCA current collector and multiple depositions enable more ErGO to be loaded, leading to a high areal capacitance. It should be noted that increasing the deposition cycles to six resulted in a maximum ErGO loading of about 0.6 mg/cm^2 on the NCAs (Figure S9). The specific capacitance of this ErGO electrode was calculated to be 160 F/g by using eq 2 (Figure S10).

In order to address the effect of the presence of NCAs, a piece of smooth Ni plate loaded with ErGO by the same method was used for control. The mass loadings of ErGO on NCAs and the Ni plate were calculated by weighing the electrode before and after

ErGO deposition. We found that the mass loading of ErGO on NCAs was almost 2 times that deposited on the bare Ni plate after the same deposition time (Figure S7d), which is conducive to the realization of high areal specific capacitance. As compared, the electrode of the ErGO on the Ni plate showed a capacitance retention of 94.3% after 20 000 cycles of CV scanning at 1000 mV/s, while that of the electrode consisting of ErGO on NCAs was recorded as high as 96.5% (Figure S7e). A Nyquist plot of the ErGO electrode is shown in Figure S7f. An equivalent circuit model (Figure S11) was used to fit the EIS data. From the inset of Figure S7f, the R_e/R_{ct} of ErGO on the NCA was 0.13/0.41 compared with 0.76/0.77 of ErGO on the Ni plate (R_e : intrinsic resistance of the substrate, the ionic resistance of the electrolyte, and the contact resistance at the ErGO/NCAs interface; R_{ct} : charge transfer resistance, which is caused by the Faradaic reactions and the double-layer capacitance on the grain surface).³⁰ A smaller R_{ct} suggests a faster charge transfer rate, which is due to the improved contact between ErGO and the NCAs.

As shown in Scheme 1, the NCAs deposited with a macroporous ErGO network after being printed with regular EVA cofferdams can be easily peeled off from the Ti plate and used as a superthin electrode. Subsequently, two ErGO electrodes coated with PVA- Na_2SO_4 gel electrolyte, eliminating the need for a separator, were carefully hot-laminated together to form an integral symmetric TGS that can light up an LED. When the supercapacitor was tailored arbitrarily, the EVA cofferdams not only function as a mechanical support to resist invasive forces and to avoid the contact of the two electrodes but also prevent the leakage of electrolyte by the closed cells. The TGS was evaluated by CV, GCD, and EIS at room temperature. From the CV curves shown in Figure 2a, it appears that the shape of the CV curves exhibited a nearly symmetric rectangle at different scan rates, indicating excellent typical double-layer capacitive characteristics. It is noteworthy that the TGS maintained an almost perfectly symmetrically rectangular shape when the scan rate rose from 50 mV/s to 5000 mV/s, and the scan rate was much higher than most of the previously reported conditions, while the capacitance retention was as high as 53%, excellently suggesting the high rate performance. Figure 2b shows a nearly ideal triangle of GCD curves when scanning at various current densities, and the IR drop calculated from the GCD curve under 0.1 mA/cm^2 was only 0.002 V, giving an equivalent series resistance (R_{ESR}) of 10 Ω/cm^2 . The areal specific capacitance of the TGS showing excellent rate performance can reach up to 6.84 mF/cm^2 , which is one of the highest values among the reported all-graphene-based supercapacitors (Figure 2c, Table S1). Figure 2d shows the volumetric capacitance of the TGS reaching up to 1.72 F/cm^3 , higher than those of some reported works,^{31–33} which is

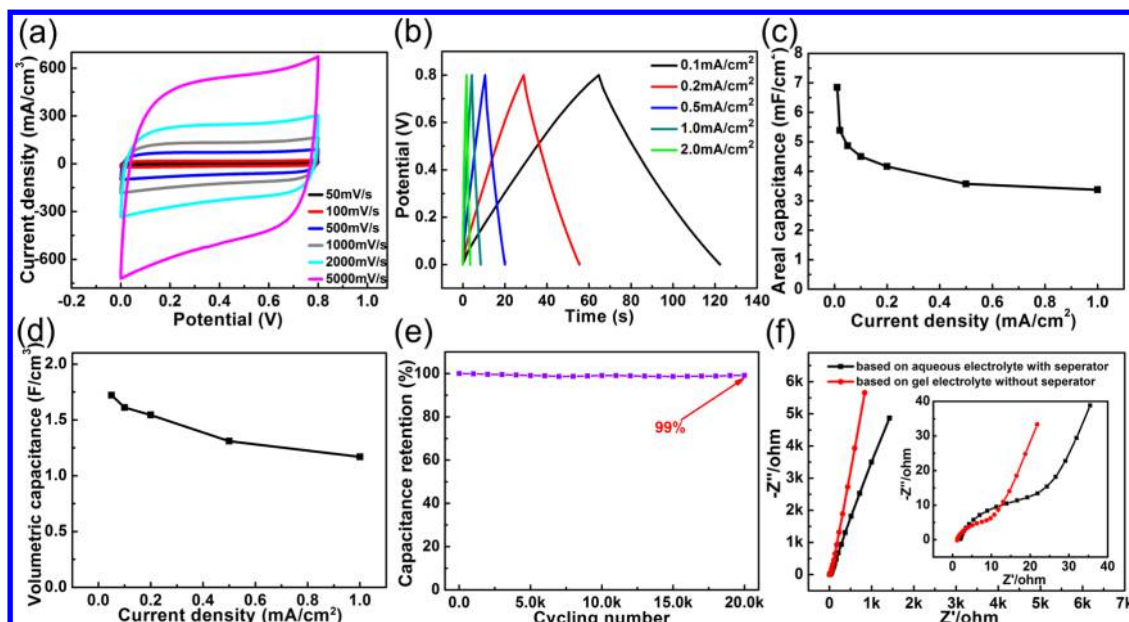


Figure 2. (a) CV curves of the TGS under different scan rates from 50 to 5000 mV/s. (b) GCD curves of the TGS with various current density ranging from 0.1 to 2.0 mA/cm². (c, d) Areal and volumetric capacitances of the TGS with different current densities. (e) Capacitance retention for the TGS that has undergone 20 000 cycles. (f) Nyquist plots of the TGS without separator and the aqueous-electrolyte-based supercapacitor with a separator; (inset) magnification of the high-frequency region.

attributable to the increased mass loading and decreased height of the TGS (about 0.045 mm, as shown in Figure S12). It is noteworthy that the thickness of ErGO should match the height of the EVA cofferdams, preventing ErGO from being deposited onto the EVA cofferdams without selectivity, which limited the improved areal and volumetric capacitance of the TGS. The cycling performance of the TGS is shown in Figure 2e. After scanning for 20 000 cycles (scan rate: 1000 mV/s), the capacitance still remained at 99%, suggesting excellent cycling stability. In order to investigate the ion mobility in this device, EIS analysis was performed and the aqueous electrolyte (pure Na₂SO₄ solution) supercapacitor fabricated with a commercial separator was used as a control sample (see Supporting Information for details). Figure 2f shows the Nyquist plots of the TGS (without separator) and the aqueous-electrolyte-based supercapacitor (with separator and without cofferdams). The former shows smaller R_e and R_{ct} , especially in the low frequency range related to Warburg resistance (W_o), indicating better EIS performance.³⁴ In order to analyze the ion mobility of the above two different systems, eq 8 was used to calculate the diffusion coefficient (D) of the ions.³⁵ The Warburg coefficients (σ) of the gel supercapacitor (without separator) and the aqueous supercapacitor (with separator) were 1922 and 2754 $\Omega/s^{1/2}$, respectively. Because D is inversely proportional to σ , the ion diffusion in the TGS without a separator was faster than the aqueous supercapacitor with a separator, which showed a more vertical curve in the Nyquist plots. The EIS study suggests that the current design of the cofferdams can excellently maintain the

ion diffusion ability in the electrolyte owing to the elimination of the commercial separator.

Volumetric energy and power densities as two important parameters for microsupercapacitors have been intensively investigated.^{36,37} A Ragone plot of the TGS and some recently reported results are shown in Figure S13. The highest energy density of the TGS reached 0.15 mWh/cm³, which is more than 2 orders of magnitude higher compared with an aluminum electrolytic capacitor³² and is comparable to graphene carbon nanotube carpet based microsupercapacitors (0.16 mWh/cm³, 1 M Na₂SO₄),³⁸ which is even higher than the laser-scribed-graphene-based supercapacitor (0.06 mWh/cm³, PVA/H₃PO₄)³² and TiN-based supercapacitor (0.05 mWh/cm³, PVA/KOH)³¹ and is slightly lower than the supercapacitor based on carbon/MnO₂ (0.22 mWh/cm³, PVA/H₃PO₄).³⁹ In addition, with the power density raised from 4 mW/cm³ to 40 mW/cm³, the retention of volumetric energy density was close to 67%, demonstrating excellent rate performance.

In order to meet the demand of broader applications, supercapacitors are often connected together in series or in parallel. Serial/parallel combinations of supercapacitors are demonstrated by connecting two TGSs together both in series and in parallel configurations with a 1.5 mA/cm² current density. As shown in Figure S14a–d, the CV and GCD curves clearly indicate that the tandem TGSs exhibited nearly ideal symmetric rectangular and triangular shapes, which were consistent with the individual TGS. Meanwhile, the operating voltage window and capacity doubled under the same test conditions, suggesting excellent consistency of each TGS. It is noteworthy that the tests for tandem

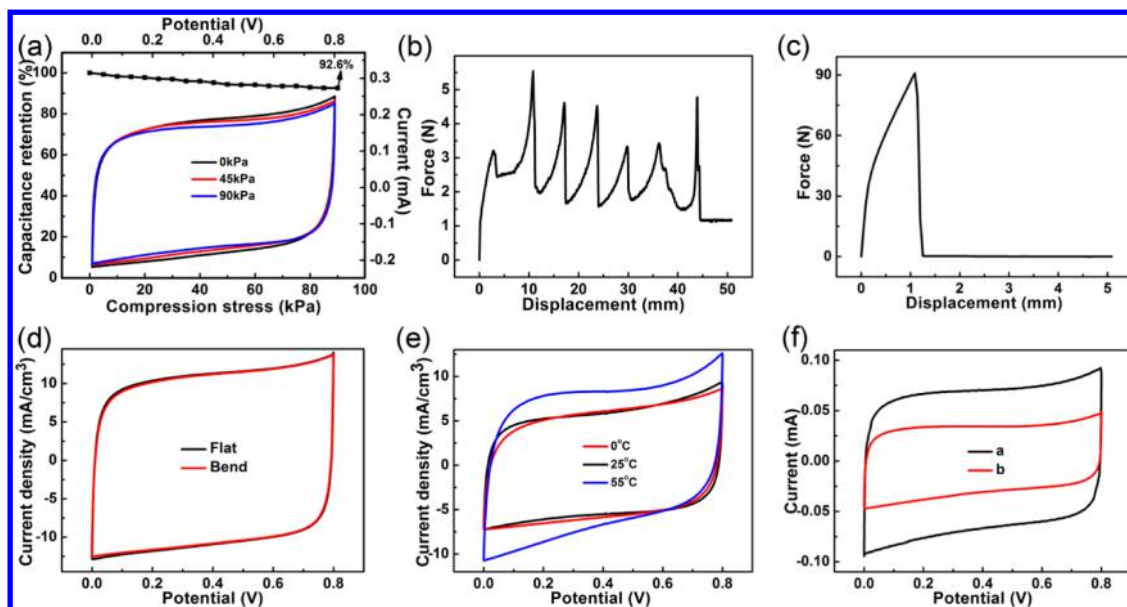


Figure 3. (a) Capacitance retention performance of the TGS under different compression strength (0, 45, and 90 kPa). (b) Force vs displacement curve of the TGS testing vehicle in a tearing test (along the direction of one of the perpendicularly printed EVA cofferdams). (c) Force vs displacement curve of the TGS testing vehicle in a lap-shear test (along the direction of one of the perpendicularly printed EVA cofferdams). (d) CV curves of the TGS tested at 100 mV/s with and without bending (curvature radius: 1.7 cm). (e) CV curves of the TGS tested at 100 mV/s at different temperatures (0, 25, and 55 °C). (f) CV curves of the TGS that correspond to the sample before (a) and after (b) being cut down to half of the size.

TGSs were performed without using a voltage balance, which was often needed with the series connections to prevent any supercapacitor from going into over-voltage.⁴⁰

For the purpose of being used in extreme conditions, a series of mechanical and temperature reliability tests were performed with the TGS. Results showed that the CV curves retained the rectangular shape under different compression stresses and the maximum compression stress applied on the TGS reached 90 kPa (capacitance retention was 92.6%), while the gel supercapacitor without EVA cofferdams (GS) broke down at 30 kPa (Figure S16a), suggesting excellent compression strength of the TGS (Figure 3a), which is comparable to that reported by Westover *et al.* for superstrong supercapacitors.⁴¹ Figure 3b,c show the curves of both tearing resistance (peeling force) and tensile (lap-shear force) tests of a TGS testing vehicle (see schematic diagram in Figure S15). In Figure 3b, six equally spaced peaks corresponded to the six parallel EVA lines that were perpendicular to the tearing direction. Figure 3c shows the typical tensile behavior of a polymer under the lap-shear conditions. The maximum tearing and lap-shear forces of the TGS testing vehicle reached 5.54 N (the stress was 2.46 MPa when only counting the EVA area) and 90.86 N (the stress was 5.05 MPa when only counting the EVA area), showing the superior mechanical property compared with the GS testing vehicle (Figure S16b,c). In order to demonstrate the flexibility of the TGS, CV curves at different bending states were measured. There was no significant change of CV curves under the bending conditions compared

to its original state, suggesting excellent flexibility (Figure 3d). In addition, the temperature reliability test (Figure 3e) showed excellent performance, as the capacitance of the TGS increased about 30% when the temperature was raised to 55 °C, corresponding to higher ionic mobility of the electrolyte at elevated temperatures. In turn, the lower ion migration at 0 °C resulted in a slightly decreased capacitance. In addition, when a piece of TGS was cut down by half of its size, the capacitance retention was 48%, which was well proportional to the area of the TGS (Figure 3f and Figure S17). The self-discharge behavior of the TGS was also studied in this work. The device was charged to V_{\max} (0.8 V) and held for 30 min, and then it took nearly 7 h for the open-circuit voltage to decrease from V_{\max} to $1/2 V_{\max}$ (Figure S18), which exceeded the reported carbon-based supercapacitor.⁴²

To demonstrate tailorability, three pieces of TGSs connected in series by stacking them together were connected to a simple circuit with a red LED (1.9 V, 30 mA) (Figure 4a; for the whole video, please refer to SI Movie-1). After charging at 3 V for 5 s, the red LED delivered a dazzling red light. Subsequently, the tandem TGSs were tailored by a pair of ceramic scissors, during and after which the LED was still lit. Meanwhile, the brightness of the LED did not show significant attenuation, implying a stable electric current flow. Since the tailoring process was during the time the LED was lit, this test strongly supported the tailorable and high safety characteristics of the TGS. Moreover, three pieces of TGSs stacked together (area of each piece: 24 cm²) and connected in series successfully

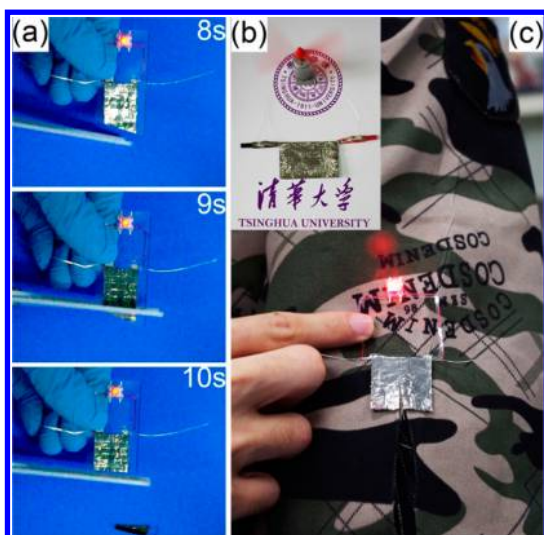


Figure 4. (a) Photographic image series that indicates TGSs being cut during working. (b) Three bigger area tandem TGSs driving a motor. (c) TGSs attached on a jacket lighting an LED indicator after being cut by a knife.

drove a minimotor with paddles (totally diameter: 9 cm), indicating excellent power density (Figure 4b). Another example of a possible application is shown by attaching three pieces of the stacked TGSs on the arm part of a jacket, which shows potential integration probability (Figure 4c). Even though both the device and the cloth are cut, the tandem TGSs could still drive an LED indicator, suggesting highly reliable power supply ability for those applications in severe conditions such as puncturing, cutting, or even experiencing a blast, which is essential in many applications.

On the basis of the above demonstrations, one can understand that when the TGS is tailored, EVA cofferdams are able to effectively prevent direct contact between the two electrodes when the device is ruptured (for comparison, both the TGS and GS were tailored, and the optical images showing their cross sections are shown in Figure S19). Additionally, even though the electrolyte inevitably leaks after the tailoring process, the gel electrolyte based on Na_2SO_4 can reduce the probability of leakage of the electrolyte and contaminations to a certain level. Furthermore, the isolated small cells originating from the EVA cofferdams can enable the electrolyte to stay in a limited area, which further prevents the leakage of electrolyte

and guarantees the functionality of the other small cells of the supercapacitor. Besides, EVA glue can also act as a binder to connect the two electrodes, which greatly simplifies the packaging process.

CONCLUSIONS

In summary, we successfully combined the macroporous ErGO network with highly ordered NCAs by a one-step electrochemical deposition process. The ErGO electrode exhibited high areal specific capacitance (57.1 mF/cm^2) and outstanding cycle stability (20 000 cycles with only 3.5% loss). In addition, compared with conventional chemical reduction, the porous ErGO layer can be homogeneously deposited on a conductive substrate and be used as the electrode without any binder; this process can be conveniently scaled up as well. Most importantly, we for the first time proposed and demonstrated the concept of a tailorable supercapacitor and proved its feasibility by using a simple stencil-printing technique. The excellent consistency, rate performance, and cycle performance (20 000 cycles with only 1% loss) of the TGS are realized. Moreover, the TGS exhibited excellent mechanical and temperature reliability, showing great potential to serve in severe conditions. In terms of the tailorable characteristic, tandem TGSs were able to drive an LED and motor work and could be attached to a cloth to prove its high reliability when they are damaged.

Given the above unique features, TGSs can meet the increasing demand of intense integration and may potentially find advanced applications in, for example, consumable and medical fields. The fabrication route of TGSs may also inspire the development of other energy storage devices. Even though both the volumetric energy/power density and size of our current supercapacitor samples were limited by the stencil-printing process and the inevitable loss of effective electrode area occupied by the cofferdams, we believe that with the advancement of printing techniques, for example nanoimprinting⁴³ and 3-D printing,^{43,44} the future tailorable energy storage devices may inherit better performances; we also envisage that the involvement of high-volumetric capacitance electrode materials and electrolytes with a wider operating voltage may sharply improve the energy density of TGSs,^{45,46} which can benefit the development of novel wearable and miniaturized devices.

EXPERIMENTAL SECTION

Synthesis of GO. The GO was prepared by a modified Hummers method.²⁸

Preparation of Nickel Nanocone Array. The nickel nanocone arrays grown on Ti foils were directly obtained by electrodeposition.²³ Nickel foam was employed as the anode, while a Ti foil with a thickness of about $40 \mu\text{m}$ was used as the cathode. First, the Ti foils and nickel foams were cleaned by

ultrasonication for 30 min in a mixed solution of acetone and ethanol (1:1 vol). Subsequently, Ti foils were coated with insulating tape, leaving an exposed area equal to $1.5 \text{ cm} \times 3 \text{ cm}$. The electrodeposition process was performed in an aqueous solution containing three components ($\text{NiCl}_2 \cdot 6\text{H}_2\text{O}$, 200 g/L, providing Ni^{2+} ; H_3BO_3 , 100 g/L, buffer agent; NH_4Cl , 40 g/L, crystal modifier, all of which are 99% pure and obtained from Sinopharm Chemical Reagent Co., Ltd.), and its pH value was adjusted to 4.0 with 10% HCl and 10% NH_4OH solutions.

In addition, the temperature of the electrolyte was maintained at 60 °C. All chemicals were used as received without further purification. The electrodeposition process was performed under 1.0 A/dm² current density for 12 min to obtain the NCAs. After that, the deposited samples were rinsed with DI water three times to remove the impurities and dried at 80 °C for 30 min.

Preparation of the ErGO Electrode. For electrochemical reduction of GO, the electrochemical deposition method was applied to obtain high-quality ErGO grown on the NCA substrates. The GO dispersion (3 mg/mL) with a 0.1 M LiClO₄ solution was used as the electrolyte. Prior to electrochemical deposition, the N₂ was constantly blown into the electrolyte to remove the O₂, which contributed to the formation of ErGO. The NCAs were used as counter electrodes, while the platinum foil acted as the working electrode. The electrodeposition was performed with a constant voltage ranging from 2.8 to 3.2 V for 20–120 min in the GO solution in a N₂ atmosphere; the mass loading of ErGO can be improved by multiplying the deposition cycles. (In our experiment, the ceiling loaded weight was about 0.6 mg/cm².) The samples were then washed carefully with DI water several times to remove the GO residue and were freeze-dried and used for further characterizations.

Fabrication of the Symmetric Supercapacitor. The symmetric TGS was fabricated by stencil printing. Ti plates with NCAs were used as current collector, and EVA (working temperature 80 °C) glue acted as the hot-melt binder. After printing, the samples were air-dried at room temperature for 1 h, which enabled the EVA glue to solidify. After the ErGO was deposited on the NCAs, the samples were cleaned with DI water. For the preparation of the gel electrolyte, Na₂SO₄ (0.5 M, 6 g) and PVA (poly(vinyl alcohol), 6 g) were added into 60 mL of deionized water, which were heated to 85 °C under stirring until the mixture became clear. The above-mentioned electrodes were uniformly coated with the gel electrolyte and air-dried for 30 min to evaporate the excess water. After that, two electrodes were carefully laminated together under a compression strength of about 8 Pa at 80 °C for 5 min. The aqueous supercapacitor with a separator was fabricated with two ErGO electrodes (area is the same as the gel supercapacitor), and a separator between the two electrodes was added to prevent a short circuit. Tape was used to package and avoid the leakage of the electrolyte.

Material Characterizations and Electrochemical Measurements. The morphologies of both NCAs and ErGO were visualized by scanning electron microscopy (SEM, Hitachi S-4800, Japan) and high-resolution transmission electron microscopy (FEIG2 spirit, Japan). The structures of the samples were studied by X-ray diffraction (XRD, RINT2000 V/PC, Bruker DS, Germany), Fourier transformation infrared spectroscopy (FTIR, Nicolet iS10, US), and Raman spectroscopy (LabRAM HR800, HORIBA Jobin Yvon, Japan). X-ray photoelectron spectroscopy (XPS) measurement (ESCALAB 250Xi, Thermo Fisher Scientific, US) was performed to analyze the surface species and chemical states of the samples. The mechanical properties were tested by an electromechanical universal testing machine (MTS, CMT6104). For the mechanical tests, Ti substrates were orthogonally stencil-printed with EVA glue and uniformly coated with PVA-Na₂SO₄ gel electrolyte, respectively, and then hot-laminated together as TGS and GS testing vehicles (dimensions: 1 cm × 2 cm). For the tearing test, the samples were tested at speeds of 500 mm/min (tearing) and 300 mm/min (tensile), respectively.

Cyclic voltammetry, galvanostatic charging/discharging, and electrochemical impedance spectroscopy of the as-prepared samples were investigated on an electrochemical station (VMP3, Bio-Logic, France) by a three-electrode configuration in a Na₂SO₄ (0.5 M) aqueous electrolyte. Platinum and saturated calomel electrodes were used as counter and reference electrodes, respectively. The applied potential window of CV and GCD was in the range from −0.8 to 0 V. The EIS was conducted in the frequency range between 100 kHz and 0.01 Hz with an amplitude of 5 mV at an open-circuit potential. The specific capacitance and area capacitance were calculated from the CV curves according to the equations below. The mass of the loaded ErGO was calculated based on a large piece of NCAs (14 cm²) electrodeposited for 30 min, and the mass of loaded ErGO was 0.14 mg.

$$C_s = \frac{\int i(V) dV}{Sv\Delta U} \quad (1)$$

$$C_m = \frac{\int i(V) dV}{mv\Delta U} \quad (2)$$

$$R_{ESR} = \frac{V_{drop}}{2i} \quad (3)$$

where C_s and C_m are the specific capacitance based on area and mass of ErGO, respectively. S is the area of the electrode, m is the mass of a single ErGO electrode, v is the scan rate, ΔU is the potential window in the CV curves, $i(V)$ is the voltammetric current, R_{ESR} is equivalent series resistance, V_{drop} is estimated from the voltage drop at the beginning of the discharge, and i is the constant current density.

For a symmetric TGS, the applied potential window of CV and GCD was in the range from 0 to 0.8 V. The total capacitance (C_{s_total} and C_{V_total}), energy (E), and power density (P) of the supercapacitor were calculated by the equations below:

$$C_{s_total} = \frac{I\Delta t}{\Delta U S} \quad (4)$$

$$C_{V_total} = \frac{I\Delta t}{\Delta U V_{total}} \quad (5)$$

$$E = \frac{C_{V_total} (\Delta U)^2}{2 \times 3600} \quad (6)$$

$$P = \frac{E}{t} \quad (7)$$

where I is the applied current, Δt is the discharge time, ΔU is the operating voltage window, V_{total} is the total volume of the TGS, including the ErGO electrode, gel electrolyte, and EVA cofferdams, and S is the specific area of supercapacitor.

To investigate the mobility of ions in the electrolyte, the diffusion coefficient (D) is qualitatively calculated by the equation below:

$$D = \frac{R^2 T^2}{2n^4 F^4 A^2 C_b^2 \sigma^2} \quad (8)$$

where D is the diffusion coefficient, A is the electrode area, C_b is the bulk concentrations of ions, and σ is the Warburg coefficient.

Conflict of Interest: The authors declare no competing financial interest.

Supporting Information Available: Figures giving (1) SEM images of NCAs; (2) Photographic images of NCAs before and after electrodeposition of ErGO; (3) XRD, FTIR, and Raman of GO and ErGO; (4) C 1s XPS spectra of GO and ErGO; (5) SEM and TEM images of ErGO deposited on NCAs; (6) SAED of GO; (7) Electrochemical results of an ErGO electrode, including CV, GCD, and EIS; (8) GCD curves of NCAs and an ErGO electrode under the same current density; (9) Mass loading of ErGO deposited on NCAs with increasing deposition cycles; (10) CV and GCD curves of a large-area ErGO electrode; (11) Equivalent circuit model; (12) Photographic image showing the thickness of the TGS; (13) Ragone plot of TGS and some reported supercapacitors; (14) CV and GCD curves for two TGSs connected in series and in parallel; (15) Schematic diagram of tearing and lap-shear test; (16) Mechanical tests of TGS and GS; (17) The photographic image of TGS after cutting down to half its size; (18) Self-discharge behavior of the TGS; (19) Optical cross section images of the TGS and GS. A table showing the comparison of areal capacitance of graphene-based supercapacitors and a movie exhibiting the tailorability of TGSs. The Supporting Information is available free of charge on the ACS Publications website at DOI: 10.1021/acsnano.5b00899.

Acknowledgment. This work is financially supported by the Shenzhen Peacock Plan No. KQCX20120814155245647, Shenzhen Technical Project No. JCYJ20130402145002411, Guangdong Province Innovation R&D Team Plan No. 2009010025, and National Nature Science Foundation of China Nos. 51202120 and 51232005.

REFERENCES AND NOTES

- Conway, B. E. *Electrochemical Supercapacitors*; Springer: Berlin, 1999.
- Simon, P.; Gogotsi, Y. Materials for Electrochemical Capacitors. *Nat. Mater.* **2008**, *7*, 845–854.
- Winter, M.; Brodd, R. J. What Are Batteries, Fuel Cells, and Supercapacitors? *Chem. Rev.* **2004**, *104*, 4245–4270.
- Meng, C.; Maeng, J.; John, S. W.; Irazoqui, P. P. Ultrasmall Integrated 3D Micro-Supercapacitors Solve Energy Storage for Miniature Devices. *Adv. Energy Mater.* **2014**, *4*, 1301269–1301276.
- Fergus, J. W. Ceramic and Polymeric Solid Electrolytes for Lithium-Ion Batteries. *J. Power Sources* **2010**, *195*, 4554–4569.
- Kamaya, N.; Homma, K.; Yamakawa, Y.; Hirayama, M.; Kanno, R.; Yonemura, M.; Kamiyama, T.; Kato, Y.; Hama, S.; Kawamoto, K. A Lithium Superionic Conductor. *Nat. Mater.* **2011**, *10*, 682–686.
- Mizuno, F.; Hayashi, A.; Tadanaga, K.; Tatsumisago, M. New, Highly Ion-Conductive Crystals Precipitated from $\text{Li}_2\text{S-P}_2\text{S}_5$ Glasses. *Adv. Mater.* **2005**, *17*, 918–921.
- Meng, C.; Liu, C.; Chen, L.; Hu, C.; Fan, S. Highly Flexible and All-Solid-State Paperlike Polymer Supercapacitors. *Nano Lett.* **2010**, *10*, 4025–4031.
- Meng, Y.; Zhao, Y.; Hu, C.; Cheng, H.; Hu, Y.; Zhang, Z.; Shi, G.; Qu, L. All-Graphene Core-Sheath Microfibers for All-Solid-State, Stretchable Fibriform Supercapacitors and Wearable Electronic Textiles. *Adv. Mater.* **2013**, *25*, 2326–2331.
- Yang, P.; Ding, Y.; Lin, Z.; Chen, Z.; Li, Y.; Qiang, P.; Ebrahimi, M.; Mai, W.; Wong, C. P.; Wang, Z. L. Low-Cost High-Performance Solid-State Asymmetric Supercapacitors Based on MnO_2 Nanowires and Fe_2O_3 Nanotubes. *Nano Lett.* **2014**, *14*, 731–736.
- Goodenough, J. B.; Kim, Y. Challenges for Rechargeable Li Batteries. *Chem. Mater.* **2009**, *22*, 587–603.
- Zhang, L. L.; Zhao, X. Carbon-Based Materials as Supercapacitor Electrodes. *Chem. Soc. Rev.* **2009**, *38*, 2520–2531.
- Geim, A. K. Graphene: Status and Prospects. *Science* **2009**, *324*, 1530–1534.
- Chen, J.; Sheng, K.; Luo, P.; Li, C.; Shi, G. Graphene Hydrogels Deposited in Nickel Foams for High-Rate Electrochemical Capacitors. *Adv. Mater.* **2012**, *24*, 4569–4573.
- Luo, J.; Jang, H. D.; Huang, J. Effect of Sheet Morphology on the Scalability of Graphene-Based Ultracapacitors. *ACS Nano* **2013**, *7*, 1464–1471.
- Chen, J.; Li, C.; Shi, G. Graphene Materials for Electrochemical Capacitors. *J. Phys. Chem. Lett.* **2013**, *4*, 1244–1253.
- Yoon, Y.; Lee, K.; Kwon, S.; Seo, S.; Yoo, H.; Kim, S.; Shin, Y.; Park, Y.; Kim, D.; Choi, J.-Y. Vertical Alignments of Graphene Sheets Spatially and Densely Piled for Fast Ion Diffusion in Compact Supercapacitors. *ACS Nano* **2014**, *8*, 4580–4590.
- Bo, Z.; Wen, Z.; Kim, H.; Lu, G.; Yu, K.; Chen, J. One-Step Fabrication and Capacitive Behavior of Electrochemical Double Layer Capacitor Electrodes Using Vertically-Oriented Graphene Directly Grown on Metal. *Carbon* **2012**, *50*, 4379–4387.
- Zhou, M.; Wang, Y.; Zhai, Y.; Zhai, J.; Ren, W.; Wang, F.; Dong, S. Controlled Synthesis of Large-Area and Patterned Electrochemically Reduced Graphene Oxide Films. *Chem.—Eur. J.* **2009**, *15*, 6116–6120.
- Peng, X.-Y.; Liu, X.-X.; Diamond, D.; Lau, K. T. Synthesis of Electrochemically-Reduced Graphene Oxide Film with Controllable Size and Thickness and Its Use in Supercapacitor. *Carbon* **2011**, *49*, 3488–3496.
- Shao, Y.; Wang, J.; Engelhard, M.; Wang, C.; Lin, Y. Facile and Controllable Electrochemical Reduction of Graphene Oxide and Its Applications. *J. Mater. Chem.* **2010**, *20*, 743–748.
- Sheng, K.; Sun, Y.; Li, C.; Yuan, W.; Shi, G. Ultrahigh-Rate Supercapacitors Based on Electrochemically Reduced Graphene Oxide for AC Line-Filtering. *Sci. Rep.* **2012**, *2*, 247–251.
- Su, Z.; Yang, C.; Xie, B.; Lin, Z.; Zhang, Z.; Liu, J.; Li, B.; Kang, F.; Wong, C. Scalable Fabrication of MnO_2 Nanostructure Deposited on Free-Standing Ni Nanocone Arrays for Ultrathin, Flexible, High-Performance Microsupercapacitor. *Energy Environ. Sci.* **2014**, *7*, 2652–2659.
- Huang, Z.-D.; Zhang, B.; Oh, S.-W.; Zheng, Q.-B.; Lin, X.-Y.; Yousefi, N.; Kim, J.-K. Self-Assembled Reduced Graphene Oxide/Carbon Nanotube Thin Films as Electrodes for Supercapacitors. *J. Mater. Chem.* **2012**, *22*, 3591–3599.
- Hang, T.; Ling, H.; Hu, A.; Li, M. Growth Mechanism and Field Emission Properties of Nickel Nanocones Array Fabricated by One-Step Electrodeposition. *J. Electrochem. Soc.* **2010**, *157*, D624–D627.
- Gao, W.; Alemany, L. B.; Ci, L.; Ajayan, P. M. New Insights into the Structure and Reduction of Graphite Oxide. *Nature Chem.* **2009**, *1*, 403–408.
- Fang, Y.; Luo, B.; Jia, Y.; Li, X.; Wang, B.; Song, Q.; Kang, F.; Zhi, L. Renewing Functionalized Graphene as Electrodes for High-Performance Supercapacitors. *Adv. Mater.* **2012**, *24*, 6348–6355.
- Lv, W.; Tang, D.-M.; He, Y.-B.; You, C.-H.; Shi, Z.-Q.; Chen, X.-C.; Chen, C.-M.; Hou, P.-X.; Liu, C.; Yang, Q.-H. Low-Temperature Exfoliated Graphenes: Vacuum-Promoted Exfoliation and Electrochemical Energy Storage. *ACS Nano* **2009**, *3*, 3730–3736.
- Li, Y.; Sheng, K.; Yuan, W.; Shi, G. A High-Performance Flexible Fibre-Shaped Electrochemical Capacitor Based on Electrochemically Reduced Graphene Oxide. *Chem. Commun.* **2013**, *49*, 291–293.
- Fan, Z.; Yan, J.; Wei, T.; Zhi, L.; Ning, G.; Li, T.; Wei, F. Asymmetric Supercapacitors Based on Graphene/ MnO_2 and Activated Carbon Nanofiber Electrodes with High Power and Energy Density. *Adv. Funct. Mater.* **2011**, *21*, 2366–2375.
- Lu, X.; Wang, G.; Zhai, T.; Yu, M.; Xie, S.; Ling, Y.; Liang, C.; Tong, Y.; Li, Y. Stabilized TiN Nanowire Arrays for High-Performance and Flexible Supercapacitors. *Nano Lett.* **2012**, *12*, 5376–5381.
- El-Kady, M. F.; Strong, V.; Dubin, S.; Kaner, R. B. Laser Scribing of High-Performance and Flexible Graphene-Based Electrochemical Capacitors. *Science* **2012**, *335*, 1326–1330.
- Zheng, H.; Zhai, T.; Yu, M.; Xie, S.; Liang, C.; Zhao, W.; Wang, S. C. I.; Zhang, Z.; Lu, X. TiO_2 @C Core-Shell Nanowires for High-Performance and Flexible Solid-State Supercapacitors. *J. Mater. Chem. C* **2013**, *1*, 225–229.
- Choi, B. G.; Hong, J.; Hong, W. H.; Hammond, P. T.; Park, H. Facilitated Ion Transport in All-Solid-State Flexible Supercapacitors. *ACS Nano* **2011**, *5*, 7205–7213.
- Qu, L.; Zhao, Y.; Khan, A. M.; Han, C.; Hercule, K. M.; Yan, M.; Liu, X.; Chen, W.; Wang, D.; Cai, Z. Interwoven Three-Dimensional Architecture of Cobalt Oxide Nanobrush-Graphene@ $\text{Ni}_x\text{Co}_{2-x}(\text{OH})_6$ for High-Performance Supercapacitors. *Nano Lett.* **2015**, *15*, 2037–2044.
- Gogotsi, Y.; Simon, P. True Performance Metrics in Electrochemical Energy Storage. *Science* **2011**, *334*, 917–918.
- Beidaghi, M.; Gogotsi, Y. Capacitive Energy Storage in Micro-Scale Devices: Recent Advances in Design and Fabrication of Micro-Supercapacitors. *Energy Environ. Sci.* **2014**, *7*, 867–884.
- Lin, J.; Zhang, C.; Yan, Z.; Zhu, Y.; Peng, Z.; Hauge, R. H.; Natelson, D.; Tour, J. M. 3-Dimensional Graphene Carbon Nanotube Carpet-Based Microsupercapacitors with High Electrochemical Performance. *Nano Lett.* **2012**, *13*, 72–78.
- Xiao, X.; Li, T.; Yang, P.; Gao, Y.; Jin, H.; Ni, W.; Zhan, W.; Zhang, X.; Cao, Y.; Zhong, J. Fiber-Based All-Solid-State Flexible Supercapacitors for Self-Powered Systems. *ACS Nano* **2012**, *6*, 9200–9206.

40. El-Kady, M. F.; Kaner, R. B. Scalable Fabrication of High-Power Graphene Micro-Supercapacitors for Flexible and on-Chip Energy Storage. *Nat. Commun.* **2013**, *4*, 2446–2454.
41. Westover, A. S.; Tian, J. W.; Bernath, S.; Oakes, L.; Edwards, R.; Shabab, F. N.; Chatterjee, S.; Anilkumar, A.; Pint, C. L. A Multifunctional Load-Bearing Solid-State Supercapacitor. *Nano Lett.* **2014**, *14*, 3197–3202.
42. Zhang, Q.; Rong, J.; Ma, D.; Wei, B. The Governing Self-Discharge Processes in Activated Carbon Fabric-Based Supercapacitors with Different Organic Electrolytes. *Energy Environ. Sci.* **2011**, *4*, 2152–2159.
43. Raut, H. K.; Dinachali, S. S.; Loke, Y. C.; Ganesan, R.; Ansah-Antwi, K. K.; Góra, A.; Khoo, E. H.; Ganesh, V. A.; Saifullah, M. S.; Ramakrishna, S. Multi-Scale Ommatidial Arrays with Broadband and Omnidirectional Anti-Reflection and Anti-Fogging Properties by Sacrificial Layer Mediated Nanoimprinting. *ACS Nano* **2015**, *9*, 1305–1314.
44. Sun, K.; Wei, T. S.; Ahn, B. Y.; Seo, J. Y.; Dillon, S. J.; Lewis, J. A. 3D Printing of Interdigitated Li-Ion Microbattery Architectures. *Adv. Mater.* **2013**, *25*, 4539–4543.
45. Tao, Y.; Xie, X.; Lv, W.; Tang, D.-M.; Kong, D.; Huang, Z.; Nishihara, H.; Ishii, T.; Li, B.; Golberg, D. Towards Ultrahigh Volumetric Capacitance: Graphene Derived Highly Dense but Porous Carbons for Supercapacitors. *Sci. Rep.* **2013**, *3*, 2975–2982.
46. Zhang, C.; Lv, W.; Tao, Y.; Yang, Q.-H. Towards Superior Volumetric Performance: Design and Preparation of Novel Carbon Materials for Energy Storage. *Energy Environ. Sci.* **2015**. Advance Article, DOI: 10.1039/C5EE00389J.